Opto-Electronic Science

Special Issue on Meta-lenses

Article

October 2024, Vol. 3, No. 10

DOI: 10.29026/oes.2024.240014

Ka-Band metalens antenna empowered by physics-assisted particle swarm optimization (PA-PSO) algorithm

Shibin Jiang[1†], Wenjun Deng[1†], Zhanshan Wang[2], Xinbin Cheng[2], Din Ping Tsai[3*], Yuzhi Shi[2*] and Weiming Zhu[1*]

Design of multiple-feed lens antennas requires multivariate and multi-objective optimization processes, which can be accelerated by PSO algorithms. However, the PSO algorithm often fails to achieve optimal results with limited computation resources since spaces of candidate solutions are quite large for lens antenna designs. This paper presents a design paradigm for multiple-feed lens antennas based on a physics-assisted particle swarm optimization (PA-PSO) algorithm, which guides the swarm of particles based on laws of physics. As a proof of concept, a design of compact metalens antenna is proposed, which measures unprecedented performances, such as a field of view at ±55°, a 21.7 dBi gain with a flatness within 4 dB, a 3-dB bandwidth >12°, and a compact design with a *f*-number of 0.2. The proposed PA-PSO algorithm reaches the optimal results 6 times faster than the ordinary PSO algorithm, which endows promising applications in the multivariate and multi-objective optimization processes, including but not limited to metalens antenna designs.

Keywords: multiple-feed lens antennas; PA-PSO algorithm; metalens; metasurfaces; Ka-band antenna.

Jiang SB, Deng WJ, Wang ZS et al. Ka-Band metalens antenna empowered by physics-assisted particle swarm optimization (PA-PSO) algorithm. *Opto-Electron Sci* **3**, 240014 (2024).

Introduction

Low Earth orbit satellite communication has the advantages of wide bandwidth, high data rates, and low latency, making low-cost compact antenna designs essential to ground terminals, such as star dishes[1]. Existing ground terminals can be divided into two categories, i.e., servo mechanism antennas and electronically scanned phased array antennas. Servo mechanism antennas are bulky and have a short lifespan, slow scanning speeds, and poor stability for real-time data transmission[2–4]. Electronically scanned phased array antennas exhibit excellent performance, but current electronic scanning methods rely on a large number of phase shifters, resulting in excessively high overall antenna costs[5–7]. Multiple-feed lens antennas can achieve wide-angle beam steering by switching the feeds located on the focal plane of the lens, which are promising candidates for low-cost ground terminals of satellite communications[8–10].

Lens antenna designs have been intensively studied, including the geometry lens[11,12], gradient-index (GRIN) lens[13–15], and metalens[16–20], etc. The geometric lens often

[1]School of Optoelectronic Science and Engineering, University of Electronic Science and Technology of China, Chengdu 610051, China; [2]Institute of Precision Optical Engineering, School of Physics Science and Engineering, Tongji University, Shanghai 200092, China; [3]Department of Electrical Engineering, City University of Hong Kong, Hong Kong 999077, China.

†These authors contributed equally to this work.

*Correspondence: DP Tsai, E-mail: dptsai@cityu.edu.hk; YZ Shi, E-mail: yzshi@tongji.edu.cn; WM Zhu, E-mail: zhuweiming@uestc.edu.cn

Received: 1 April 2024; Accepted: 24 May 2024; Published online: 26 July 2024

results in a limited field of view (FOV) and a bulky size due to its curved focal plane and large *f*-number. Although non-planar lenses such as 3D Luneburg lenses can achieve large-angle beam scanning, their feed antennas require conformal shaping, making the antennas less integrated[21–23]. Additionally, non-planar lenses may block the electromagnetic waves from adjacent antennas when the beam steering angle is large. For example, the FOV of the spherical Luneburg lens antenna is quite limited when forming a tight coupling antenna array. More importantly, non-planar lenses rely on expensive and time-consuming fabrication technologies such as 3D printing, which significantly increases their costs. Planar GRIN lenses highly rely on the choices of materials with low loss tangent and variable permittivity, resulting in high costs and limited functionalities.

Metasurfaces, as two-dimensional artificial electromagnetic materials, tailor the incident wavefront through sub-wavelength unit structures, resulting in compact sizes and light weights[24–29]. More importantly, metasurfaces offer substantial design flexibilities to accommodate incident wavefronts, making them promising candidates for multiple-feed lens antennas. Recently, lens antennas based on metasurfaces, which are named metalens antenna, have been prevalently explored. In 2015, N. J. G. Fonseca introduced a non-circular symmetrical lens design capable of achieving a 50° scanning angle, but this design required the rotation of the lens itself to achieve the 360° beam scanning[30]. In 2016, K. Pham designed a transmissive lens capable of ±30° scanning, yet without a significant breakthrough in scanning angle[31]. In 2019, H. F. Wang designed a parabolic-shaped metalens with a scanning angle of ±60°, but the overall gain of the lens was relatively low, with approximately 18.5 dBi at 0° and only around 15 dBi at 60°[32]. Albeit the great importance, the design of metalens antenna with a compact size, large FOV, small *f*-number, and high gain remains a great challenge.

Performances of multiple-feed lens antennas rely on the designs of lenses, which vary from different functionalities. Firstly, the lens must accommodate different incident wavefronts from different feeds in terms of overall gain and its flatness crossing the entire FOV. Secondly, the 3-dB angle bandwidth and the number of feeds must be carefully planned to avoid the blind zone within the FOV of the lens antenna. Finally, the cost and compactness of the multiple-feed lens antennas are highly dependent on their lens designs, such as *f*-number of the lenses, choices of lens materials, and fabrication processes of lenses, etc. Therefore, metalens antenna designs are highly dependent on multivariate and multi-objective optimization processes, which can be effectively improved using PSO algorithms.

The PSO is an optimization method that finds the best solution in the search space by moving a population of candidate solutions, named particles, based on a mathematical formula over the position and velocity of the particle[35]. Therefore, the PSO is a good candidate for the optimization of metalens antenna, which has large design flexibilities, i.e., large solution spaces. However, the PSO is a metaheuristic procedure, which does not guarantee the optimal solution. In other words, the PSO may lead to a sub-optimal solution by directing the swarm of particles towards the closest extrema conditions.

Here, we propose a design paradigm for metalens antenna based on a physics-assisted particle swarm optimization (PA-PSO) algorithm. The solution space of the metalens design has been greatly reduced by applying the rotational symmetry and maximum gain conditions of the metalens phase distribution. As a result, computation resources for the optimization process are greatly reduced. More importantly, the swarm of particles is guided by the maximum gain conditions, giving rise to the less possibility of finding a sub-optimal solution and reduced computation time. As a proof of concept, we demonstrate a compact and wide FOV metalens antenna design, which measures nontrivial performances with an FOV of ±55°, *f*-number of 0.2, a 21.7 dBi gain with a flatness within 4 dB, and a 3-dB bandwidth >12°. Compared with the traditional PSO algorithm, the PA-PSO algorithm finds the optimal metalens antenna design using 1/6 computation time, which shows promising applications not only in metalens antenna but also in many other meta-devices designs requiring multivariate and multi-objective optimization processes.

Metalens design based on PA-PSO algorithm

The proposed multiple-feed metalens antenna consists of a metalens and a feed array, as shown in Fig. 1(a, b). The metalens is composed of unit cells whose positions can be described using the polar coordinates $UP(\alpha, r)$, as shown in Fig. 1(a). The beam steering function of the metalens antenna is realized by switching the feeds. Therefore, the lens antenna emission angle can be described using the elevation angle θ and azimuth angle ϕ

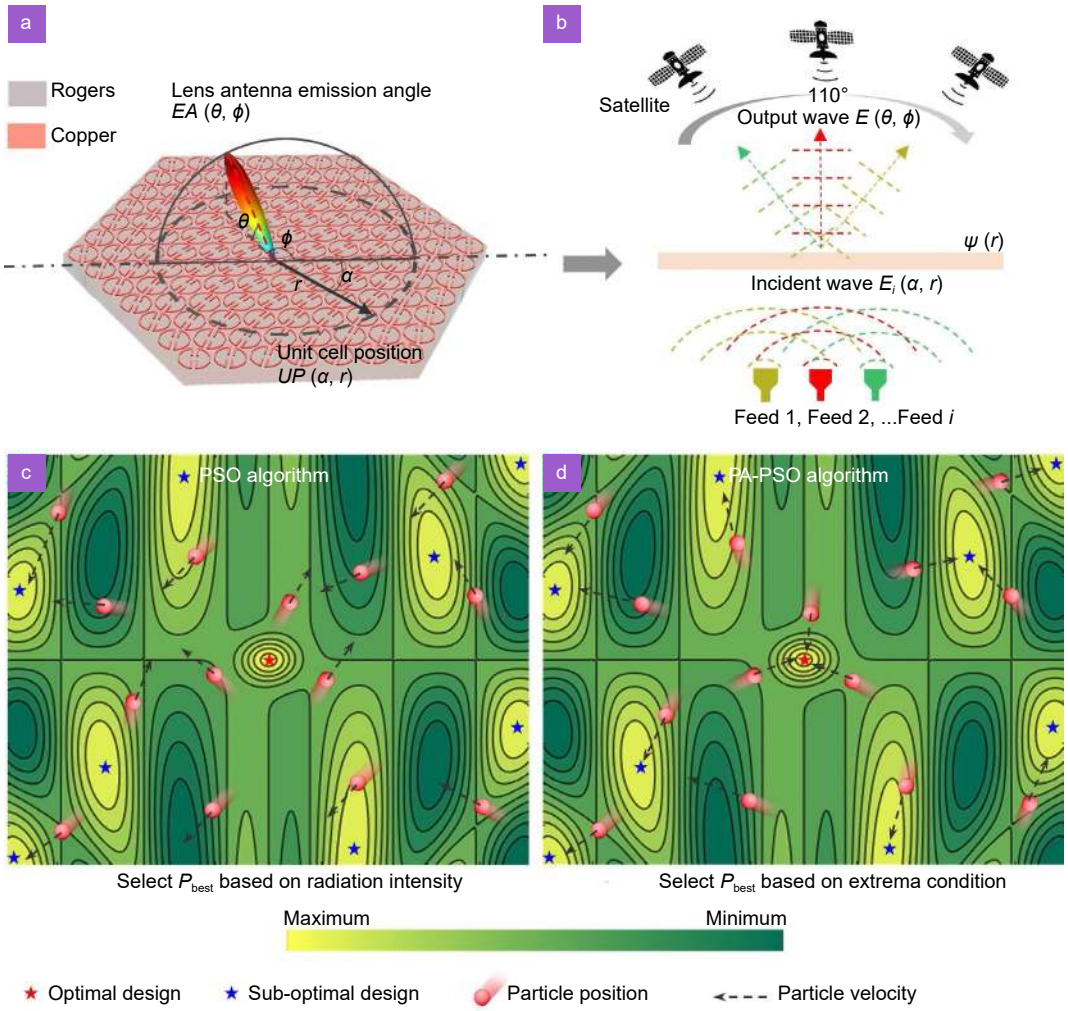

Fig. 1 | Schematics of the PA-PSO algorithm. (**a**) and (**b**) Working principle of the metalens antenna. (**c**) and (**d**) Comparison between the traditional PSO and PA-PSO algorithm. The red and blue stars represent optimal and sub-optimal designs, respectively. The red dots and dashed arrows represent the positions and velocities of the particles, respectively. (c) The working principle of the PSO algorithm where the swarm of particles is guided by the radiation intensity. (d) The PA-PSO algorithm guides the swarm of particles based on the extrema condition of the radiation intensity, which shows the correct directions of the maximum radiation intensity. This approach guides the swarm of particles more efficiently, which reduces not only the computation time but also the likelihood of finding sub-optimal designs.

of deflection beams, i.e., $EA(\theta,\ \phi)$.

The metalens coverts incident wavefronts from different feeds, i.e., Feed 1 … Feed *i*, into planar ones whose deflection angles depend on the location of the feeds, as shown in Fig. 1(b). Here, the incident waves from Feed *i* on the metalens can be described by the spatial distribution of the incident electromagnetic waves,

$$E_i(\alpha, r) = A_i e^{j(\omega t+\varphi_i(\alpha,r))}\ , \qquad (1)$$

where A_i and φ_i are the amplitude and phase of incident waves, respectively.

The incident waves can be tuned by the unit cells independently in terms of both phase and amplitude. The metalens design has a solution space of the size M^N where M is the set of all possible unit cell selections and N is the number of the metalens unit cells. The solution space of a metalens design is quite large, considering the choice of the unit cells is typically larger than 4 to cover a 2π phase change and the number of the unit cells is more than 1000, i.e., $M > 4$ and $N > 1000$. In this paper, two assumptions are made to reduce the solution space for the sake of the practical computation time. One is that the transmission coefficients of the unit cells are unity to minimize the insertion loss of the metalens, i.e., all unit cells have the same amplitude modulation. The other is that the metalens has rotational symmetry which is the same as the feed array. Therefore, the metalens design can be described by its phase profile, i.e., $\varphi_m(r)$. The

output wavefront from the metalens can be written as,

$$E_{\rm m} = E_i {\rm e}^{\varphi_{\rm m}(r){\rm j}} \ . \tag{2}$$

The subwavelength unit cell can be considered a point source whose radiation pattern can be decomposed to planar waves with uniform amplitudes. Considering a certain emission angle $EA(\theta,\ \phi)$ the planar wave component emitted from a unit cell located at $UP(\alpha,\ r)$ can be expressed as,

$$E_{\rm o}(\alpha, r) = A_{\rm s}(\theta, \phi) E_{\rm m} {\rm e}^{-\boldsymbol{k}\cdot\boldsymbol{r}{\rm j}} \ , \tag{3}$$

where $A_s(\theta, \phi)$ is the weight of the planar wave determined by the scattering properties of the unit cells, $\boldsymbol{k}$ is the wavevector of the planar waves, and $\boldsymbol{r}$ is the displacement of the unit cell from the center of the metalens. $-\boldsymbol{k}\cdot\boldsymbol{r}$ is the planar wave phase retardation due to the location of the unit cells. Here, $A_{\rm s}(\theta, \phi)$ is a constant due to the point source approximation of the unit cell.

Therefore, the electromagnetic radiation of the metalens antenna can be expressed as the integration of the planar waves from all unit cells,

$$E(\theta, \phi) = A_{\rm s} \int_0^R r \int_0^{2\pi} A_i(\alpha, r) {\rm e}^{{\rm j}(\omega t + \varphi_i(\alpha, r) + \varphi_{\rm m}(r) - \boldsymbol{k}\cdot\boldsymbol{r})} {\rm d}\alpha {\rm d}r \ , \tag{4}$$

where R is the radius of the metalens, $\boldsymbol{k}$ is a function of θ and ϕ, and $\varphi_i(\alpha, r)$ is determined by the incident wavefront. Therefore, the radiation intensity I of the metalens antenna at a given θ and ϕ can be written as a function of metalens design $\varphi_{\rm m}(r)$,

$$\begin{aligned} I(\varphi_{\rm m}(r)) =& E(\varphi_{\rm m}(r)) \cdot E(\varphi_{\rm m}(r))^* \\ =& \left[\int_0^R r {\rm e}^{\varphi_{\rm m}(r){\rm j}} \varepsilon(r) {\rm d}r\right] \cdot \left[\int_0^R r {\rm e}^{\varphi_{\rm m}(r){\rm j}} \varepsilon(r) {\rm d}r\right]^* \ , \end{aligned} \tag{5}$$

where E^* is the conjugate of E and $\varepsilon(r) = \int_0^{2\pi} A_s A_i(\alpha, r) {\rm e}^{{\rm j}[\omega t + \varphi_i(\alpha, r) - \boldsymbol{k}\cdot\boldsymbol{r}]} {\rm d}\alpha$ determined by both the incident wavefront and the emission angle of the metalens antenna. Therefore, $I(\varphi_m(r))$ can be written as,

$$\begin{aligned} I(\varphi_m(r)) = & \left[\int_0^R r {\rm e}^{[\varphi_m(r) + phase(\varepsilon(r))]{\rm j}} |\varepsilon(r) {\rm d}r|\right] \cdot \\ & \left[\int_0^R r {\rm e}^{[\varphi_m(r) + phase(\varepsilon(r))]{\rm j}} |\varepsilon(r) {\rm d}r|\right]^* . \end{aligned} \tag{6}$$

The extrema condition of I can be derived by using the variational method detailed in Supplementary information, which are

$$\varphi_m(r) + phase(\varepsilon(r)) = constant \ , \tag{7}$$

$$\text{or} \qquad E(\varphi_{\rm m}(r)) = \int_0^R {\rm e}^{\varphi_{\rm m}(r){\rm j}} \varepsilon(r) {\rm d}r = 0 \ . \tag{8}$$

Eqs. (7) and (8) represent the maximum and minimum conditions of metalens antenna radiation intensity, respectively.

The physical implication is that the optimal value is attained when the sum of the phase modulation provided by the unit structures on each ring and the accumulated phase propagation in the direction of light propagation on each ring remains constant. In other words, the incident electromagnetic waves on each ring of the metasurface, when integrated over the ring in the direction, result in a coherent and constructive addition of the field for each ring.

The extrema condition reveals the relationship between the metalens design $\varphi_m(r)$ and the incident waves from different feeds $\varepsilon(r)$, which are the solution space and the initial conditions of the optimization algorithm, respectively. The phase of each ring that is served as a particle in the PSO algorithm is optimized individually, ensuring that all rings have the same phase in the direction of 55°. Here, the PSO method is chosen for the metalens antenna optimization algorithm, whose optimization targets include the compactness (f-number), FOV, and gain. The criterion is to maximize the radiation intensity when f-number ≤ 0.2 and FOV ≥ ±50°.

Figure 1(c, d) show the working principles of the traditional PSO algorithm and the PA-PSO algorithm. The red and blue stars represent optimal and sub-optimal designs, respectively. The red dots and dashed arrows represent the positions and velocities of particles, respectively. The traditional PSO algorithm guides the swarm of particles using the radiation intensity, while the PA-PSO algorithm guides the swarm of particles based on the extrema condition as shown in Eq. (7). The extrema condition shows correct directions of the maximum radiation intensity. Supplementary information Fig. S1 shows the flow diagram of the traditional PSO and PA-PSO algorithms, respectively. For a fair comparison, the only difference between the PSO and PA-PSO algorithms is highlighted in the flow diagram with red-dashed lines. The maximum iteration of both algorithms is set to be 5000 to compare the algorithm convergence speed.

As shown in Fig. 2(a), compared with the PSO algorithms, the PA-PSO algorithms decouple the optimization of each ring while utilizing the particle swarm optimization algorithm's search capability for the optimal

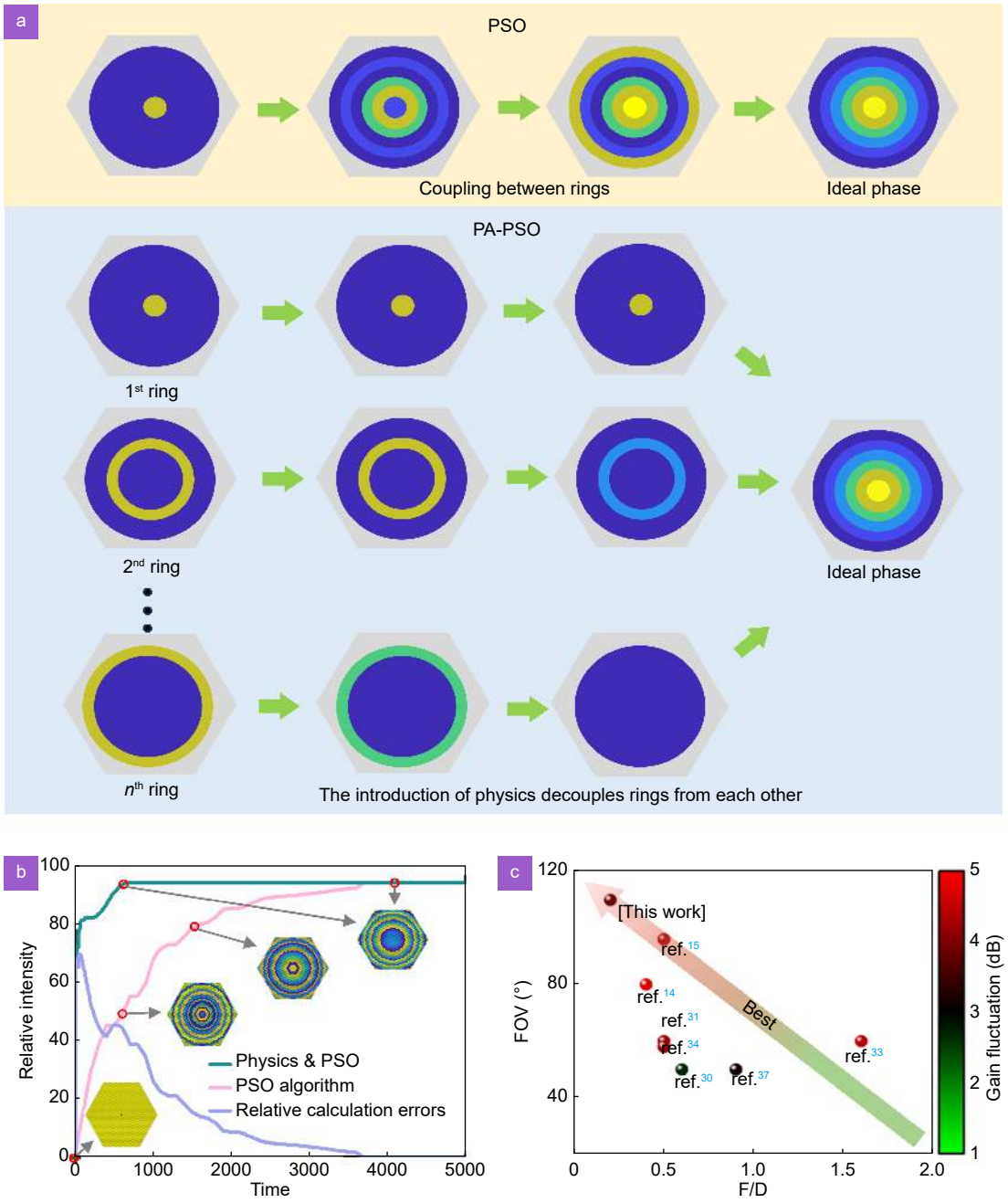

Fig. 2 | Architecture and performance of the PA-PSO algorithm. (**a**) Difference between PSO and PA-PSO algorithms. The yellow background in the image represents the optimization process of the PSO algorithm. During this optimization process, the phase changes between the rings are coupled, requiring more iteration time. The blue background indicates that after introducing physics, the optimization between the rings is decoupled, and they do not influence each other. As a result, the number of optimization iterations naturally decreases. (**b**) Variation of the relative electric field intensity with respect to the times of iteration for PA-PSO and PSO algorithms. The purple line shows the calculation errors. The four hexagons from bottom to top represent phase distributions at different stages: initial phase distribution, PSO algorithm iteration 650 times, PSO algorithm iteration 1500 times, and PSO algorithm iteration 4100 times (PA-PSO algorithm iteration 650 times). (**c**) Comparison of FOVs and F/D for planar lens antennas. The colors of the points indicate the fluctuation of gains when scanning within the field of view range.

values. Figure 2(b) shows the optimization speed of both algorithms evaluated by using the times of the iteration. Given the widespread use of the PSO algorithm in practical engineering optimizations, we conduct a comparison between the PA-PSO and PSO algorithms in terms of the radiation intensity, which is a critical parameter for the design of metalens antenna. To quantify differences between the two algorithms, we define calculation errors

based on their respective radiation intensity outputs. Although the extremum condition serves as the criterion for determining the optimality of the PA-PSO algorithm, we still calculate the energy emitted in a specific direction by the entire lens after each iteration for the purpose of comparison. The results, depicted in Fig. 2(b), show an interesting trend: initially, the calculation error increases rapidly when the iteration count is less than 65. This suggests that the PA-PSO algorithm converges to the optimal solution more quickly than the standard PSO algorithm. Subsequently, the calculation error decreases as the radiation intensity improvement between adjacent iterations diminishes when approaching the optimal solution. Our final optimization results reveal that the relative intensity achieved by the PA-PSO algorithm is 94.62806, while for the PSO algorithm, it is 94.62786. As the interaction count approaches 5000, the calculation error tends to zero, signifying the convergence of both algorithms. Consequently, the PA-PSO algorithm demonstrates significantly lower computational cost while achieving optimization results identical to the widely used PSO algorithm. However, the PA-PSO algorithm reaches the best state after 650 times of iteration while the traditional PSO algorithm costs 4100 times of iteration, i.e., more than six times of computation time compared with PA-PSO. Therefore, the PA-PSO approach guides the swarm of particles more efficiently, which reduces not only the computation time but also the likelihood of finding sub-optimal designs.

Metalens antenna design and characterization results

The design parameters of the metalens antenna are shown in Fig. 3(a). The feeds array is located on the focal plane of the metalens, which is 22 mm away from the metalens surface, i.e., F = 22 mm. The displacement x of the feeds is defined by the distance between the feed and the central axis of the metalens. The radius of the metalens R is 55 mm. The f-number of the metalens is defined by the ratio of the focal length F and the lens diameter,

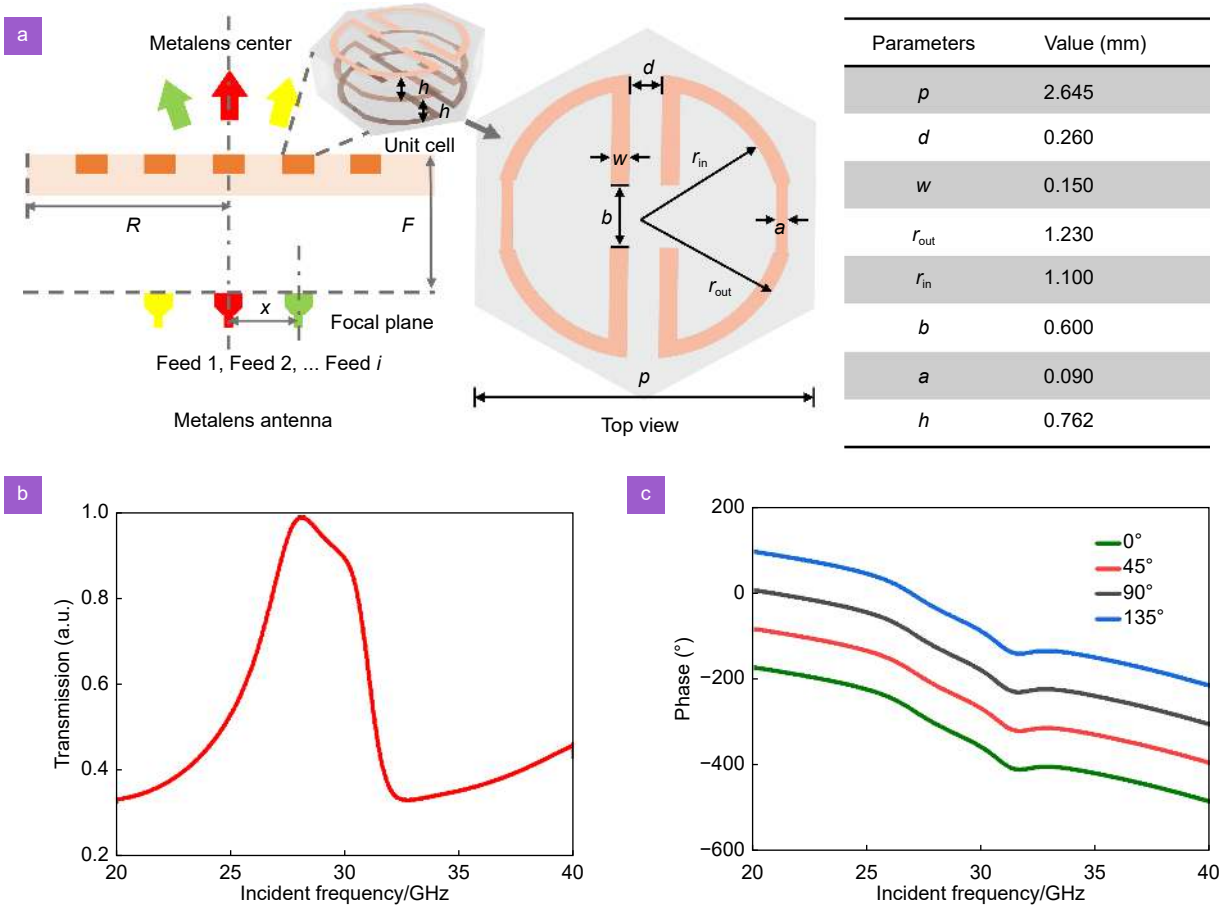

Parameters	Value (mm)
p	2.645
d	0.260
w	0.150
r_{out}	1.230
r_{in}	1.100
b	0.600
a	0.090
h	0.762

Fig. 3 | Design and Characteristics of the metalens antenna. (**a**) Design parameters of the unit structure of the metalens antenna. (**b**) Transmission spectrum of the unit cells. (**c**) Phase spectra of unit cells when the unit cell is rotated with respect to the fast axis of the left circularized incident light.

i.e., *F*/2*R*, which is the same as geometric lenses. Therefore, the *f*-number of the proposed metalens is 0.2, indicating a compact design of the metalens antenna.

A Pancharatnam-Berry unit cell structure is chosen for the metalens design to accommodate the incidence with circular polarization states[36]. The unit cell structure has three layers of identical metal structures spaced by two dielectric layers (Rogers 4350b) with a permittivity of 3.2 and a thickness *h* of 0.762 mm. Detailed design parameters of the metal layer can be found in the inserted table of Fig. 3(a). The multiple-layer design of the unit cell structure enables a high transmission and a 2π phase modulation of the incident EM waves with a frequency range of 27 to 30 GHz, which is shown in Fig. 3(b, c), respectively. Here, the unit cells are rotated with respect to the fast axis of the left circularized incidence to cover the 2π phase modulation.

A microstrip antenna design is chosen for the feeds of the metalens antenna (see Fig. S2). As shown in Fig. S2(c), the output wavefront of the feed antenna is similar to a point source, which has a 3-dB angular bandwidth of 110°. Figure S2(b) shows that return loss of the feed is low within the frequency region, ranging from 27 to 30 GHz.

The metalens antenna is characterized by a microwave near-field scanning system, as shown in Fig. 4(a), which is composed of an Agilent N5247A vector network analyzer (VNA), two VNA header extenders at Ka-band (one transmitter and one receiver), and a WR-28 open waveguide as a probe. RF absorbers are also used to avoid reflections between the instrumentation. The lens is placed between the WR-28 waveguide and the feed, which is assembled in the focal plane of the lens. The displacement *x* of the feed is regulated by a mechanic frame as shown in Fig. 4(b). As a result, the feed displacement *x* can be chosen from 0, 5 mm, 10 mm, 15 mm, 20 mm, 25 mm, and 30 mm using different mounting positions on the focal plane. The receiving WR-28 is placed at 100 mm behind the metalens to perform the 2D near-field measurement, as shown in Fig. 4(d).

Figure 5 shows the measured gain profiles of the metalens antenna with different feed displacements *x* when the incident frequency is 28.5 GHz. Figure 5(a–c) show the comparison between the experimental (blue lines) and simulation results (red lines) when the displacement is 0, 15 mm, and 30 mm, respectively. The experimental results agree well with the simulation results obtained using the finite-difference time-domain method. Figure 5(d)

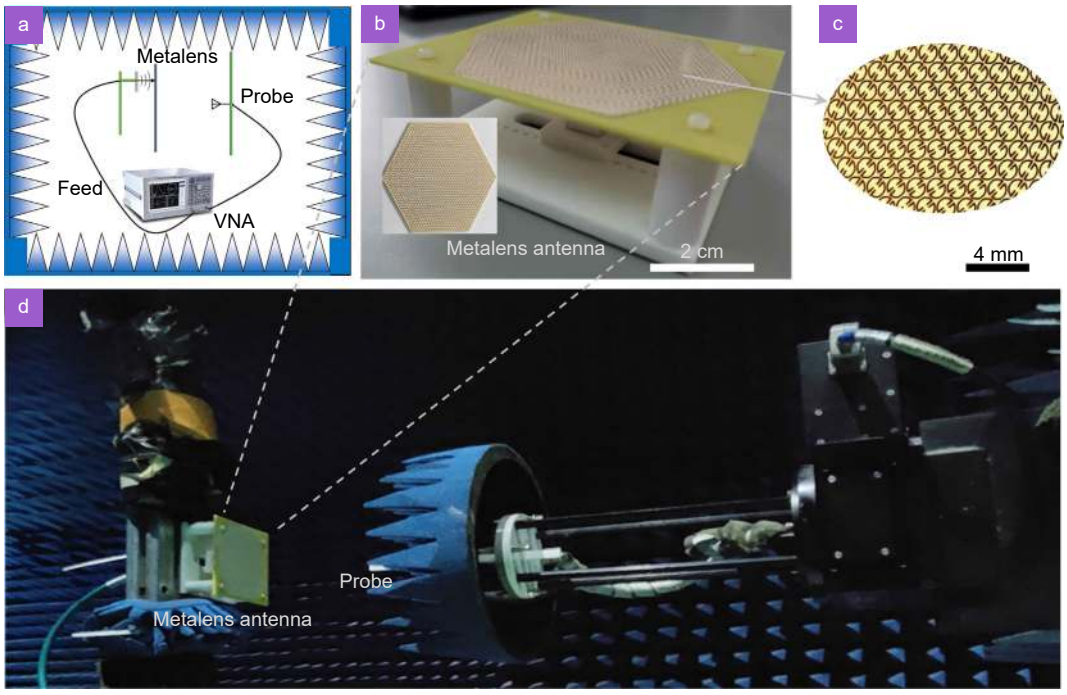

Fig. 4 | Device fabrication and experimental setup. (**a**) Schematic of the experimental setup for near-field measurement. (**b**) The fixture and metasurface lens antenna used in the test. The bottom of the fixture holds the feed source antenna and includes insertable holes to alter the position of the feed source. The distance from the feed source to the metasurface lens is 2.2 cm. (**c**) A enlarged view of the metamaterial lens. (**d**) Photograph of the experimental setup. The experimental setup consists of probes, assembled feed source antenna, metasurface lens, and a vector network analyzer connecting the probes and feed source antenna.

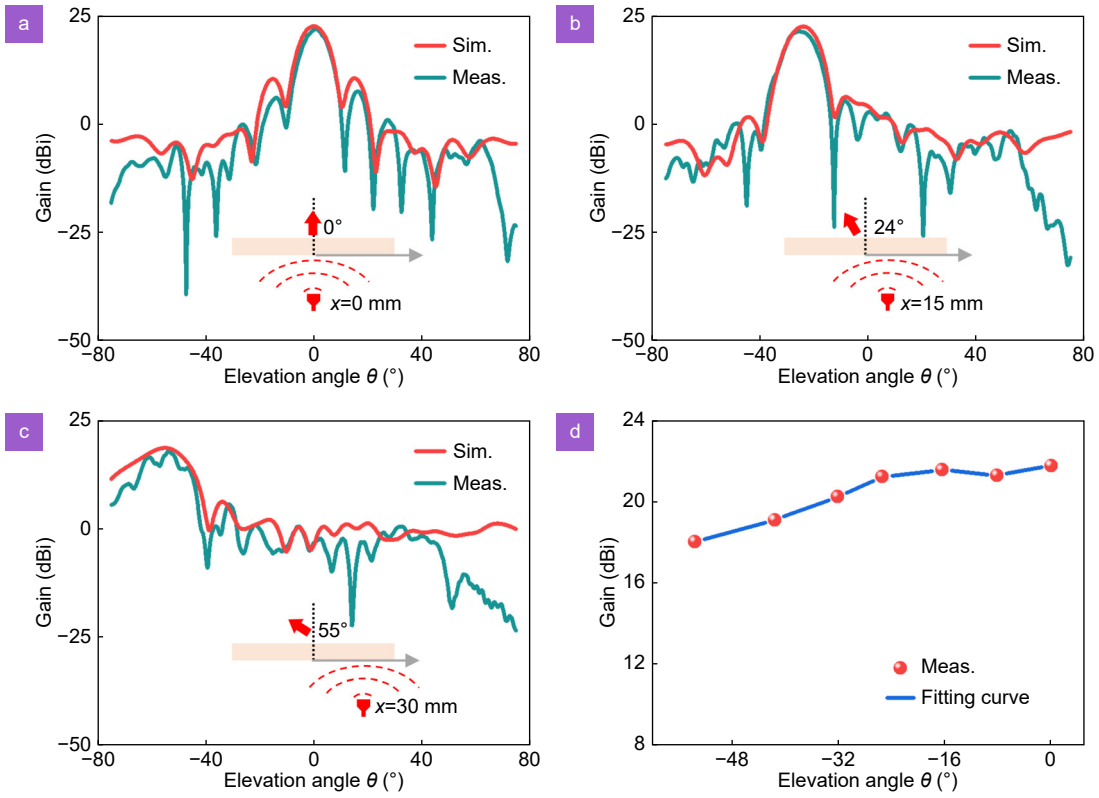

Fig. 5 | Gain profiles of the metalens antenna when the feed is placed on the focal plane with different displacements *x*. Comparison between the experimental results (blue lines) and simulation results (red lines) when the feed source position is (**a**) at x = 0, showing a maximum gain of 21.7 dBi, which corresponds to an angle of 0°; (**b**) at x = 15 mm, showing a maximum gain is 21.2 dBi, which corresponds to an angle of 25°; (**c**) at x = 30 mm, showing a maximum gain is 18.3 dBi, which corresponds to an angle of 55°. (**d**) The relationship between the maximum gain angles and the corresponding gains obtained from testing the feed source at different positions.

shows the measured max gain when the feed displacement varies from 0 to 30 mm. The elevation angle is changed from 0° to 55°, indicating an FOV of ±55°. The gain reaches 21.7 dBi when the displacement x is 0, and the flatness of the gain is within 4 dB. The gain profiles of different displacements can be found in Supplementary Fig. S3. The metalens antenna is designed to operate within a frequency band spanning from 27 to 30 GHz. Our selection of the feed antenna is a patch antenna widely used in phased array antennas[38–40]. Notably, this patch antenna exhibits a reflection loss of less than 10% across the entire range of 27 to 30 GHz (as shown in Fig. S2(b)). Additionally, the radiation pattern remains stable within this frequency band (Fig. S2(c)). However, it is important to note that the axial ratio of the feed antenna varies significantly with the frequency and radiation angle (as demonstrated in Fig. S2(d)). Consequently, the gain fluctuation from 27 to 30 GHz is limited to within 5 dB, as indicated in Fig. S4. In Fig. S5, we observe that within a 15-degree range, there is a polarization isolation exceeding 10 dB. Similarly, within a 41-degree range, the polarization isolation remains at 6 dB. However, as the angle increases beyond these ranges, the polarization isolation gradually decreases to 3 dB. This reduction is primarily attributed to the energy emitted at large angles from the feed source, which lacks favorable axial ratios, leading to a diminished polarization isolation.

Table 1 shows a comparison between different types of lens antennas with beam steering functions. The proposed metalens design has superb performances in terms of compactness and FOV when compared with other metalens antenna designs. The overall performance of the metalens antenna is comparable with and somewhere better than the planar lens antennas, as seen in Fig. 2(c). In comparison with existing configurations of planar lens antennas characterized by f-number, FOV, and scanning losses, the proposed metalens antenna design stands out as a significant advancement. With an eminently low f-number of 0.2, the focal length is optimized for compactness while maintaining efficient incident wave gathering. Notably, the metalens demonstrates a wide FOV of ±55°, surpassing many configurations in

Fig. 2(c) and rendering it highly versatile for applications requiring extensive angular coverage. The optimization process, guided by the PA-PSO algorithm, minimizes scanning loss by prioritizing maximum gain conditions. In contrast to diverse tradeoffs existing in other configurations, the proposed metalens antenna achieves a compelling balance in various critical characteristics. Notably, the metamaterial lens design proposed in ref.[32] adopts a parabolic phase distribution, which exhibits a relatively low efficiency. Under nearly equivalent aperture conditions, the 0-degree gain of this design can reach 21.7 dBi, whereas the parabolic design only achieves 18.5 dBi. Additionally, the parabolic design leads to difficulties in enlarging the lens size[41], a challenge not present in the design proposed in this paper. Furthermore, due to the effective decoupling of interactions between rings achieved by the proposed algorithm, there is a distinct advantage in optimizing large-sized lenses. In the case of an n-ring lens, with coupling present, there are n^Q possible phase distributions (where Q is the number of phases being searched). After decoupling, there are only $n{\cdot}Q$ possible phase distributions. Therefore, the introduction of physics effectively reduces the optimization scope, especially in the optimization process of large-sized lenses.

Table 1 | The comparison between different types of lens antennas with beam steering function.

Lens type	FOV	F	Ref.
Luneburg Lens	±55°	NA	ref.[21]
	±61°	NA	ref.[22]
Grin Lens	±48°	0.5	ref.[15]
	±40°	0.4	ref.[14]
Metalens	±55°	0.2	This work
	0°–50°	<1	ref.[37]
	0°–50°	0.55	ref.[30]

Conclusions

In summary, this paper proposes a nontrivial PA-PSO optimization method for designing multiple-feed metalens antennas. The proposed method guides the speed and velocity of particles based on the extrema condition of the metalens design, giving rise to a much faster optimization process for the metalens antenna design. As a proof of concept, a design of compact metalens antenna is proposed and compared with the existing lens antennas, showing superior antenna performances in terms of FOV, gain, compactness, low cost, etc. However, metalens antennas exhibit a tradeoff between the overall efficiency and the FOV, resulting in relatively lower aperture efficiencies compared to their counterparts based on phased arrays. Specifically, the aperture efficiency is 17% at the central frequency, i.e., 28.5 GHz. Nevertheless, when compared to other metalens designs with similar FOVs[32], our scheme demonstrates a significant improvement in aperture efficiency. This improvement is substantiated by an overall 3 dB gain across the entire FOV. Crucially, we expect that by integrating the patch antenna design into the PA-PSO algorithm, we can optimize both the broadband performance and the polarization isolation of the metalens antenna within the frequency range from 27 to 30 GHz.

This innovative algorithm, enriched by the infusion of physics principles, not only navigates the expansive solution spaces inherent in multivariate and multi-objective optimization but does so with an exceptional efficiency. Its accelerated convergence makes it particularly well suited for resource-intensive tasks, making a notable impact on the pace of design exploration and refinement. As a testament to its prowess, the PA-PSO algorithm is applied to the design paradigm of multiple-feed lens antennas, where it not only overcomes limitations of traditional PSO algorithms but also achieves notable results in a fraction of the time. The proposed compact metalens antenna, designed under the guidance of PA-PSO, sets new benchmarks with a wide field of view, high gain, flatness, and a bandwidth exceeding expectations. Its compact form factor, characterized by a low f-number, further attests to the ability of the algorithm to deliver superior performance within constrained spatial requirements.

In essence, this paper not only introduces a cutting-edge optimization algorithm but also demonstrates its prowess through a tangible application in antenna design. The accelerated optimization process opens avenues for its use in diverse fields beyond metalens antennas, positioning the PA-PSO algorithm as a transformative force in advancing solutions for complex multivariate and multi-objective optimization challenges. The proposed metalens antenna, characterized by its wide field of view, compact design, and optimized scanning capabilities, holds significant promise across diverse applications in contemporary electromagnetic systems. In communication systems, the efficiency of the metalens antenna in capturing incident waves over a broad angular

range positions it as an ideal candidate for next-generation wireless communication and satellite technologies. Furthermore, the metalens antenna is well feasible for radar systems, 5G networks, and the Internet of Things. The unique attributes of the metalens antenna, guided by the innovative PA-PSO algorithm, pave the way for enhanced performance and efficiency in electromagnetic systems, marking a noteworthy advancement in the realm of applied electromagnetics.

References

1. Yue PY, An JP, Zhang JK et al. Low earth orbit satellite security and reliability: issues, solutions, and the road ahead. *IEEE Commun Surv Tutor* **25**, 1604–1652 (2023).
2. Fkirin MA, Khira MAE. Enhanced antenna positioning control system using adapted DC servo motor and Fuzzy-PI controller. *IEEE Access* **11**, 102661–102668 (2023).
3. Duan XC, Qiu YY, Mi JW et al. On the mechatronic servo bandwidth of a Stewart platform for active vibration isolating in a super antenna. *Robot Comput Integr Manuf* **40**, 66–77 (2016).
4. Debruin J. Control systems for mobile Satcom antennas. *IEEE Control Syst Mag* **28**, 86–101 (2008).
5. Sadhu B, Tousi Y, Hallin J et al. A 28-GHz 32-element TRX phased-array IC with concurrent dual-polarized operation and orthogonal phase and gain control for 5G communications. *IEEE J Solid-State Circuits* **52**, 3373–3391 (2017).
6. Zhao K, Helander J, Sjoberg D et al. User body effect on phased array in user equipment for the 5G mmWave communication system. *IEEE Antennas Wirel Propag Lett* **16**, 864–867 (2017).
7. Maguid E, Yulevich I, Veksler D et al. Photonic spin-controlled multifunctional shared-aperture antenna array. *Science* **352**, 1202–1206 (2016).
8. Hao RS, Zhang JF, Jin SC et al. K-/Ka-band shared-aperture phased array with wide bandwidth and wide beam coverage for LEO satellite communication. *IEEE Trans Antennas Propag* **71**, 672–680 (2023).
9. Lee J, Kim H, Oh J. Large-aperture metamaterial lens antenna for multi-layer MIMO transmission for 6G. *IEEE Access* **10**, 20486–20495 (2022).
10. Qu ZS, Qu SW, Zhang Z et al. Wide-angle scanning lens fed by small-scale antenna array for 5G in millimeter-wave band. *IEEE Trans Antennas Propag* **68**, 3635–3643 (2020).
11. Ansarudin F, Abd Rahman T, Yamada Y et al. Multi beam dielectric lens antenna for 5G base station. *Sensors* **20**, 5849 (2020).
12. Wang C, Wu J, Guo YX. A 3-D-printed multibeam dual circularly polarized Luneburg lens antenna based on quasi-icosahedron models for *Ka*-band wireless applications. *IEEE Trans Antennas Propag* **68**, 5807–5815 (2020).
13. Zhang N, Jiang WX, Ma HF et al. Compact high-performance lens antenna based on impedance-matching gradient-index metamaterials. *IEEE Trans Antennas Propag* **67**, 1323–1328 (2019).
14. Hernandez CAM, Elmansouri M, Filipovic DS. High-directivity beam-steerable lens antenna for simultaneous transmit and receive. In *2019 IEEE International Symposium on Phased Array System & Technology* 1–5 (IEEE, 2019); http://doi.org/10.1109/PAST43306.2019.9020904.
15. Imbert M, Romeu J, Baquero-Escudero M et al. Assessment of LTCC-based dielectric flat lens antennas and switched-beam arrays for future 5G millimeter-wave communication systems. *IEEE Trans Antennas Propag* **65**, 6453–6473 (2017).
16. Wang Y, Fan Q, Xu T. Design of high efficiency achromatic metalens with large operation bandwidth using bilayer architecture. *Opto-Electron Adv* **4**, 200008 (2021).
17. Deng W, Jiang S, Shi Y et al. Mid - infrared dynamic wavefront transformer based on a two - degrees - of - freedom control system. *Laser Photonics Rev* **16**, 2200152 (2022).
18. Zhu RC, Wang JF, Qiu TS et al. Remotely mind-controlled metasurface via brainwaves. *eLight* **2**, 10 (2022).
19. Feng ZW, Shi T, Geng GZ et al. Dual-band polarized upconversion photoluminescence enhanced by resonant dielectric metasurfaces. *eLight* **3**, 21 (2023).
20. Nan T, Zhao H, Guo J et al. Generation of structured light beams with polarization variation along arbitrary spatial trajectories using tri-layer metasurfacess. *Opto-Electron Sci* **3**, 230052 (2024).
21. Biswas S, Lu A, Larimore Z et al. Realization of modified Luneburg lens antenna using quasi-conformal transformation optics and additive manufacturing. *Microw Opt Technol Lett* **61**, 1022–1029 (2019).
22. Li YJ, Ge L, Chen ME et al. Multibeam 3-D-printed Luneburg lens fed by magnetoelectric dipole antennas for millimeter-wave MIMO applications. *IEEE Trans Antennas Propag* **67**, 2923–2933 (2019).
23. Liu KN, Yang SW, Qu SW et al. Phased hemispherical lens antenna for 1-D wide-angle beam scanning. *IEEE Trans Antennas Propag* **67**, 7617–7621 (2019).
24. Zhang F, Pu MB, Li X et al. Extreme-angle silicon infrared optics enabled by streamlined surfaces. *Adv Mater* **33**, 2008157 (2021).
25. Ha YL, Luo Y, Pu MB et al. Physics-data-driven intelligent optimization for large-aperture metalenses. *Opto-Electron Adv* **6**, 230133 (2023).
26. Zhang HC, Zhang X, Ma XL et al. Full-space beam scanning based on transmission reflection switchable quadratic phase metasurface. *Opt Express* **30**, 36949–36959 (2022).
27. Guo YH, Zhang ZJ, Pu MB et al. Spoof plasmonic metasurfaces with catenary dispersion for two-dimensional wide-angle focusing and imaging. *iScience* **21**, 145–156 (2019).
28. Shi YZ, Song QH, Toftul I et al. Optical manipulation with metamaterial structures. *Appl Phys Rev* **9**, 031303 (2022).
29. Gao H, Fan XH, Wang YX et al. Multi-foci metalens for spectra and polarization ellipticity recognition and reconstruction. *Opto-Electron Sci* **2**, 220026 (2023).
30. Lima EB, Matos SA, Costa JR et al. Circular polarization wide-angle beam steering at Ka-band by in-plane translation of a plate lens antenna. *IEEE Trans Antennas Propag* **63**, 5443–5455 (2015).
31. Pham K, Nguyen NT, Clemente A et al. Design of wideband dual linearly polarized transmitarray antennas. *IEEE Trans Antennas Propag* **64**, 2022–2026 (2016).
32. Wang HF, Wang ZB, Wu ZH et al. Beam-scanning lens antenna based on elliptical paraboloid phase distribution metasurfaces. *IEEE Antennas Wirel Propag Lett* **18**, 1562–1566 (2019).
33. Lou Q, Chen ZN. Sidelobe suppression of metalens antenna by

amplitude and phase controllable metasurfaces. *IEEE Trans Antennas Propag* **69**, 6977–6981 (2021).
34. Jiang M, Chen ZN, Zhang Y et al. Metamaterial-based thin planar lens antenna for spatial beamforming and multibeam massive MIMO. *IEEE Trans Antennas Propag* **65**, 464–472 (2017).
35. Jain M, Saihjpal V, Singh N et al. An overview of variants and advancements of PSO algorithm. *Appl Sci* **12**, 8392 (2022).
36. Liu YJ, Zhang AX, Xu Z et al. Wideband and low-profile transmitarray antenna using transmissive metasurface. *J Appl Phys* **125**, 045103 (2019).
37. Matos SA, Lima EB, Silva JS et al. High gain dual-band beam-steering transmit array for satcom terminals at Ka-band. *IEEE Trans Antennas Propag* **65**, 3528–3539 (2017).
38. Weigand S, Huff GH, Pan KH et al. Analysis and design of broad-band single-layer rectangular U-slot microstrip patch antennas. *IEEE Trans Antennas Propag* **51**, 457–468 (2003).
39. Ansari JA, Brij Ram R. Analysis of broad band U-slot microstrip patch antenna. *Microw Opt Technol Lett* **50**, 1069–1073 (2008).
40. Lee KF, Luk KM, Mak KM et al. On the use of U-slots in the design of dual-and triple-band patch antennas. *IEEE Antennas Propag Mag* **53**, 60–74 (2011).
41. Pu MB, Li X, Guo YH et al. Nanoapertures with ordered rotations: symmetry transformation and wide-angle flat lensing. *Opt Express* **25**, 31471–31477 (2017).

Acknowledgements

This work was supported by the National Natural Science Foundation of China (61975026, 62375232, 62375232 62205246 and 61875030), Creative Research Groups of the National Natural Science Foundation of Sichuan Province (2023NSFSC1973), the Shanghai Pilot Program for Basic Research, the National Key Research and Development Program of China (No. 2023YFF0613600), and Science and Technology Commission of Shanghai Municipality (No. 22ZR1432400).

Author contributions

WM Zhu proposed the original idea and supervised the project. SB Jiang and WJ Deng designed the samples and performed the measurements. YZ Shi, ZS Wang, and XB Cheng fabricated the samples. DP Tsai, YZ Shi, and WM Zhu co-wrote the paper. All authors discussed and commented on the paper.

Competing interests

The authors declare no competing financial interests.

Supplementary information

Supplementary information for this paper is available at https://doi.org/10.29026/oes.2024.240014

Scan for Article PDF